PERGAMON International Journal of Multiphase Flow 24 (1998) 1383–1406

International Journal of Multiphase Flow

Turbulent flow past a bubble and an ellipsoid using shadow-image and PIV techniques

A. Tokuhiro [a,*], M. Maekawa [b], K. Iizuka [b], K. Hishida [b], M. Maeda [b]

[a] *Reactor Engineering Safety, Power Reactor and Nuclear Fuel Development Corp., Oarai Engineering Center, Oarai, Ibaraki 311-13, Japan*

[b] *Department of Mechanical Engineering, Keio University, 3-14-1 Hiyoshi, Kohoku-ku, Yokohama, 223 Japan*

Received 19 April 1997; received in revised form 23 March 1998

Abstract

An experimental investigation on flow around an oscillating bubble and solid ellipsoid with a flat bottom was conducted. A single air bubble (equivalent diameter $D_e = 9.12$ mm) was attached to a small disk (~1 mm) at the end of a needle and suspended across a vertical square channel (100 mm) by wire wherein water flowed downward at a constant flowrate. The solid ellipsoid ($D_e \sim 9.1$ mm) was suspended across the square channel in the same manner. The equivalent diameter-based Reynolds and Eotvos number range, $1950 < Re < 2250$ and $11 < Eo < 11.5$, placed the bubble in the 'wobbly' regime while the flow in its wake was turbulent. A constant flowrate and one bubble size was used such that flow in the wake was turbulent. Velocity measurements of the flow field around the bubble or solid were made using a one CCD camera Digital Particle Image Velocimetry (DPIV) system enhanced by Laser Induced Fluorescence (LIF). The shape of the bubble or solid was simultaneously recorded along with the velocity using a second CCD camera and an Infrared Shadow Technique (IST). In this way both the flow-field and the boundary of the bubble (solid) were measured. The velocity vector plots of flow around and in the wake of a bubble/solid, supplemented by profiles and contours of the average and root-mean-square velocities, vorticity, Reynolds stress and turbulent kinetic energy, revealed differences in the wake flow structure behind a bubble and solid. One of the significant differences was in the inherent, oscillatory motion of the bubble which not only produced vorticity in the near-wake, but as a result of apparent vorticity stretching distributed the turbulent kinetic energy associated with this flow more uniformly on its wake, in contrast to the solid.

Keywords: Digital particle image velocimetry (DPIV); Laser induced fluorescence (LIF); Infrared shadow technique (IST); Single-bubble; Turbulent wake flow; Bubble oscillations

* Corresponding author.

0301-9322/98/$19.00
PII: S0301-9322(98)00024-X

1. Introduction

The study of flow around a solid body such as an ellipsoid or that around a single rising gas bubble in a volume of liquid are two classic examples of problems in fluid mechanics of single- and multi-phase flows. It goes without saying that from an understanding of such rudimentary systems, one often extrapolates this knowledge, for better or worse, to larger systems such as fluidized-beds, bio-reactor bubble columns and other equipment involving solid–liquid, gas–liquid and even solid–gas–liquid flows. Our base of knowledge on the fundamental aspects of bubbles, drops and particles accumulated over many years are contained in such texts as those by Levich (1962) and Clift et al. (1978).

In the present experimental investigation we are interested in developing a measurement technique to measure the flow around a single-bubble or its solid, similarly-shaped equivalent within a flow channel. The measurement technique is aimed at extracting velocity information not only of the flow of liquid, but includes identification, as well as detection of movement and distortion of the gas–liquid boundary. Additionally while many investigations have been carried out on a single bubble rising in a quiescent liquid, the present work is carried out in a vertical flow channel with downward flow of water. As for velocity measurement techniques employed in the past, they mainly encompass a wide variety of (classic) flow visualization techniques, mainly photographic and cinematic, or pointwise measurement within the flow field, such as by hot-film/hot-wire anemometry, laser Doppler velocimetry and impedance or optically-based phase detection probes. While these techniques provide valuable data in a classic sense, recent developments in processing of image-based data enables the investigator to further quantify and combine the aforementioned visualization and velocity measurement techniques.

We thus sought to apply a number of recent and now widely available measurement techniques (in contrast to the classic) in unison to the fundamental problem of flow around bubbles and in this case, a similarly-shaped solid equivalent. Specifically the flow conditions, our objectives were thus two-fold: (1) to explore the applicability of DPIV, LIF and a specifically developed shadow technique to this problem; and (2) to evaluate the information content produced by our measurement system; that is, to note the differences in the wake flow structure of flow around a solid and a bubble. In order to facilitate measurement of velocity information a small surface was provided onto which a bubble could attach itself as water flowed downward rather than having a freely rising bubble in counterflow. In the authors opinion such an arrangement still simulates a 'real' system with bubbly flows where grids or other surfaces are encountered (and to which bubbles attach themselves) just as other bubbles may freely rise in the same system. Thus the relevance and importance of the present arrangement, though not identical to a free bubble system, seems self-evident.

2. Measurement method

In order to detect the interaction between the bubble motion (or the solid ellipsoid) and the turbulent flow field which it encounters, we implemented a Digital Particle Image Velocimetry (DPIV) system previously described by Sakakibara et al. (1993a,b). The hardware components

of our DPIV measurement system consisted of the following: (1) a 4W Ar-ion laser (INNOVA 70); (2) a charge coupled device (CCD) camera (SONY XC-77RR, NTSC 768×493 pixel); and (3) a timing counter to synchronize the laser and camera (built in-house). The acoustic optical modular (AOM) cell chops the laser beam (Hoya Model 1-60) and is synchronized to the vertical signal of the CCD camera. The video signal was recorded on a VTR (Panasonic AG-700, S-VHS, NTSC) with each frame encoded with a unique bar code (24 bits binary, 8×8 pixels black or white). Our original intent was to simultaneously capture both the bubble and tracer particle motions, the latter of which was approximately 1000 times smaller in size than the bubble. However, it became clear that the intensity of light reflected from the bubble's surface saturated the CCD camera such that the intensity of light from the tracer particles was overwhelmed. We thus resorted to application of Laser Induced Fluorescence (LIF) using fluorescent particles (1–10 μm) with a specific density 1.02 along with a light-sheet produced by optical lenses; that is, by mixing tracer particles with rhodamine-B we could detect the fluorescence emitted by the particles through a color filter (to cut reflections) into our CCD camera. We found that with this set-up we could detect the motion of tracer particles in the vicinity of the bubble–liquid interface. The test media were air for the bubble and water as the continuous medium.

Next, in order to measure the bubble's shape and motion we supplemented the DPIV-LIF system with an infrared shadow-image technique (IST) specifically prepared for this experiment. Fig. 1 thus depicts our arrangement consisting of two CCD cameras; one for DPIV-LIF (rear camera) and the other for IST (front). A shadow of the bubble (or solid) was produced from infrared LEDs outlining a square and located behind the bubble. The emitted light was filtered through a translucent cover-sheet and produced a shadow of the bubble (or solid) which was then captured by the front CCD camera. In order to capture both the bubble shape and the flow field around it simultaneously, we synchronized the triggering of the laser, the LEDs and the two CCD cameras. The laser sheet is shown to enter the test section from the right side.

As for the experimental apparatus it consisted of two rectangular tanks, a lower and upper, connected in between by a vertical, channel of $100 \times 100\,\text{mm}^2$ and 1000 mm in length. A schematic is shown in Fig. 2. At the top of the channel there is an entrance section to the test section with a grid in order to generate a homogenous turbulent incoming flow. Water thus flowed downward through the channel to the lower tank where it was pumped back up to the upper tank. The mid-region of the channel was our measurement section and consisted of a side-port from where either a bubble or solid model made of polyamine epoxy plaster, could be introduced. We note that several solid models, as well as several kinds of polyamine epoxies and resins were used. The average, measured density of the solid was 2095 kg/m^3. The bubble or solid was attached to a small disk (dia. 1–2 mm) located at the end of a stiff needle (length 78 mm) which itself was suspended across the channel by a piano-wire in tension. The small disk was centered within the square cross-section of the channel. We noted that in the case of the bubble, the surface tension force was of sufficient magnitude (though unmeasured) to keep the bubble attached to the small disk at all times for the data shown here. In other words the bubble did not detach itself or 'float' momentarily during the measurement. Otherwise without the disk, it was difficult to keep a bubble suspended at the axial location of measurement whilst maintaining a constant turbulent flow at the entrance. Earlier studies by Davidson and

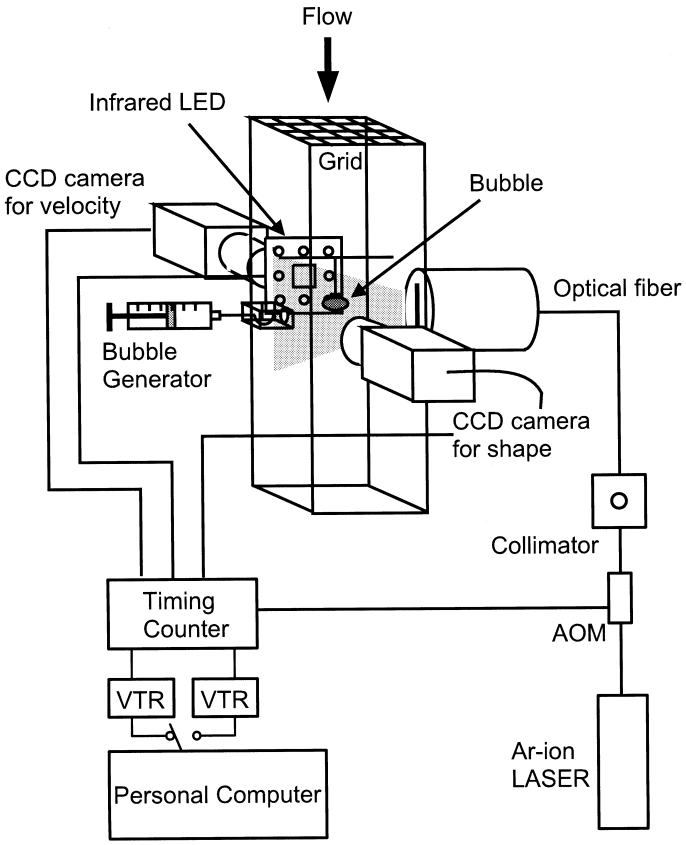

Fig. 1. Schematic of the DPIV, LIF and IST systems used for measurement.

Kirk (1969), Moo-Young et al. (1971) and Kojima et al. (1975) each used flow tailoring or contoured entrance sections not only to fix an entrance flow profile but, by doing so, kept a bubble quasi-stationary. We did not want this for lack of generality of the entrance flow conditions. So, the small disk provided a surface onto which the bubble could attach itself while water flowed past it. In fact, the terminal rise velocity of a free bubble in our channel was measured to be on average, 24.5 cm/s. The downward flow velocity specified in Moo-Young et al., corresponding to the equivalent diameter of our bubble is within 10% of that specified in the present experiment. So the operational flowrate was held constant at $U_{\mathrm{avg}} = 0.245$ m/s, while the corresponding turbulent intensity level due solely to grid-generated turbulence was ~3% in the channel. This level was measured separately by laser Doppler velocimetry (LDV). As for the reference bubble size used in the presentation of our data, each bubble was introduced using a syringe volume of V = 0.4 ml, corresponding to an equivalent bubble diameter of $D_{\mathrm{e}} \doteqdot 9.12$ mm. This figure was independently verified by a calculation of the breadth from a correlation put forth by Tadaki and Maeda (1961) based on the flow and physical properties. The solid model was an ellipsoid with a major diameter $D_{\mathrm{major}} = 12$ mm, minor diameter $D_{\mathrm{minor}} = 5.8$ mm, but with a flat bottom of diameter, $d = 10$ mm. The model was solid throughout.

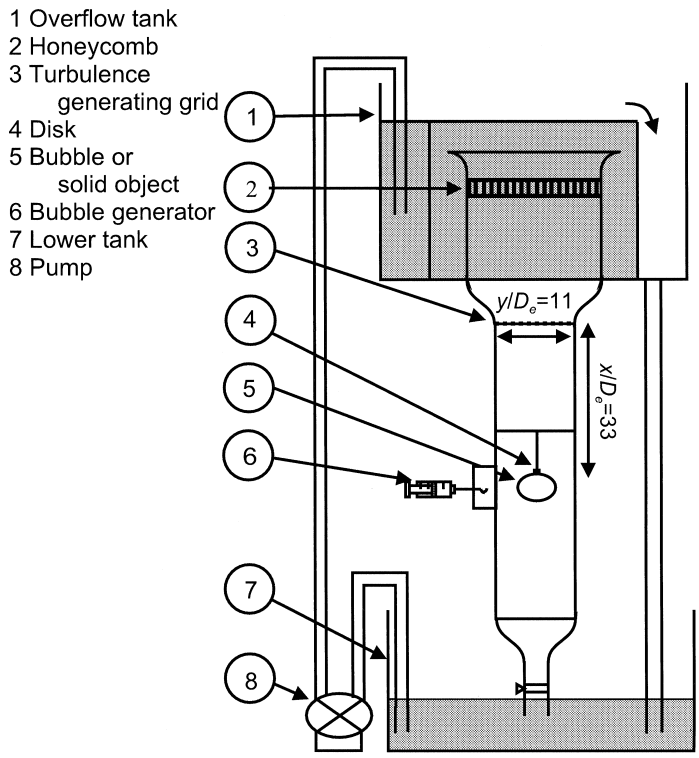

Fig. 2. Schematic of experimental loop.

3. Results

Figure 3 shows a representative still image of the bubble's shadow (in black) imposed on a grayscale background. The bubble in the figure is *right-shifted* in a descriptive sense and has been captured at one instant during a continuous oscillatory motion in all three axial directions. The bubble is attached at the top (center) to a small disk that appears as a squarish region, from which a vertical stem representing the needle can also be seen. Figure 4 depicts a representative image of the tracer particles, including a partial outline of the bubble boundary and the region inside which contains a few speckles (in the background). Note especially in the latter figure that there is a white region located at the top. This appears to be a region of high light reflectance that saturates the CCD camera's field of view. Because the laser sheet is bright, it is very difficult to eliminate reflections from various surfaces such that the image is completely saturation free.

Based on these and similar images for a solid ellipsoid, we extracted velocity information from a collection of 1000 images. Other velocity-related information were subsequently calculated. For initial comparison, we present in Figs. 5 and 6 the extent of the measured flow field around the bubble and solid. The boundary of the bubble and solid are represented in approximate form by solid lines. Note that tracer particles imaged behind the bubble and errant particles in front of the solid generate some meaningless vectors within the respective boundaries. Because the laser sheet enters from the left and a region of relatively larger

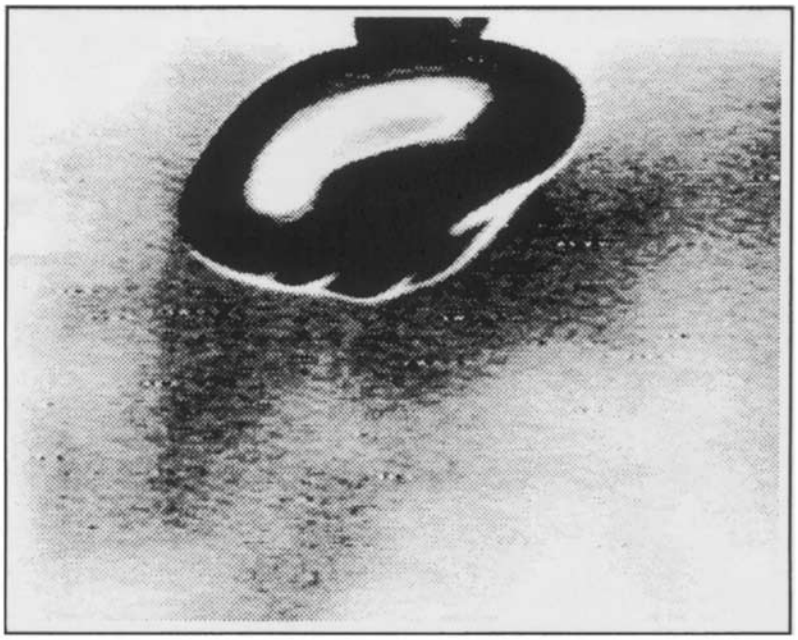

Fig. 3. Typical snapshot image of bubble as captured by IST.

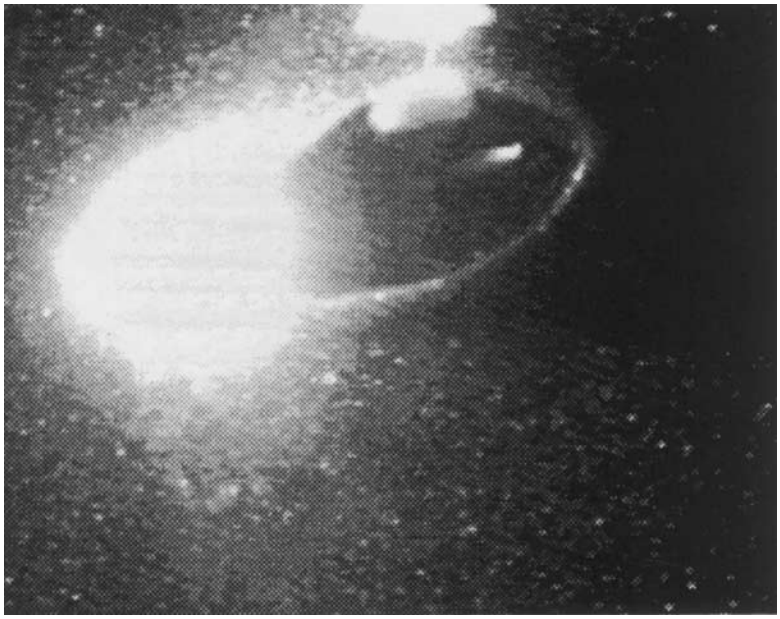

Fig. 4. Typical snapshot image of bubble and particles as captured by DPIV and LIF.

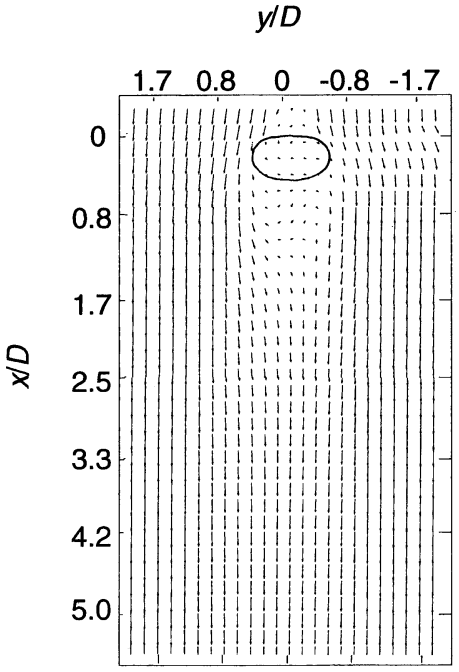

Fig. 5. Representative vector field plot of the flow around the bubble.

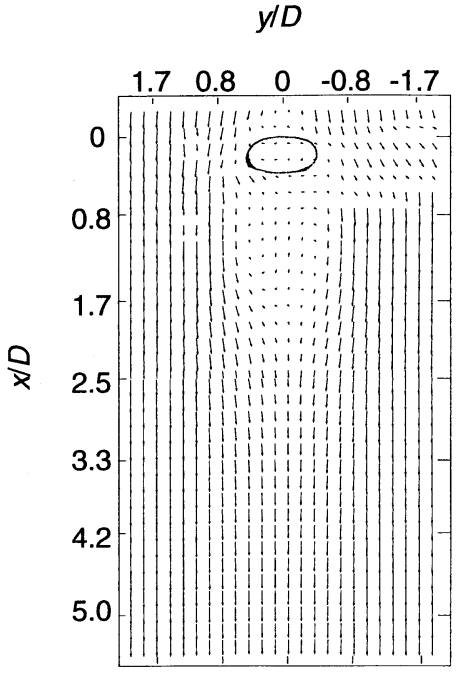

Fig. 6. Representative vector field plot of the flow around the solid.

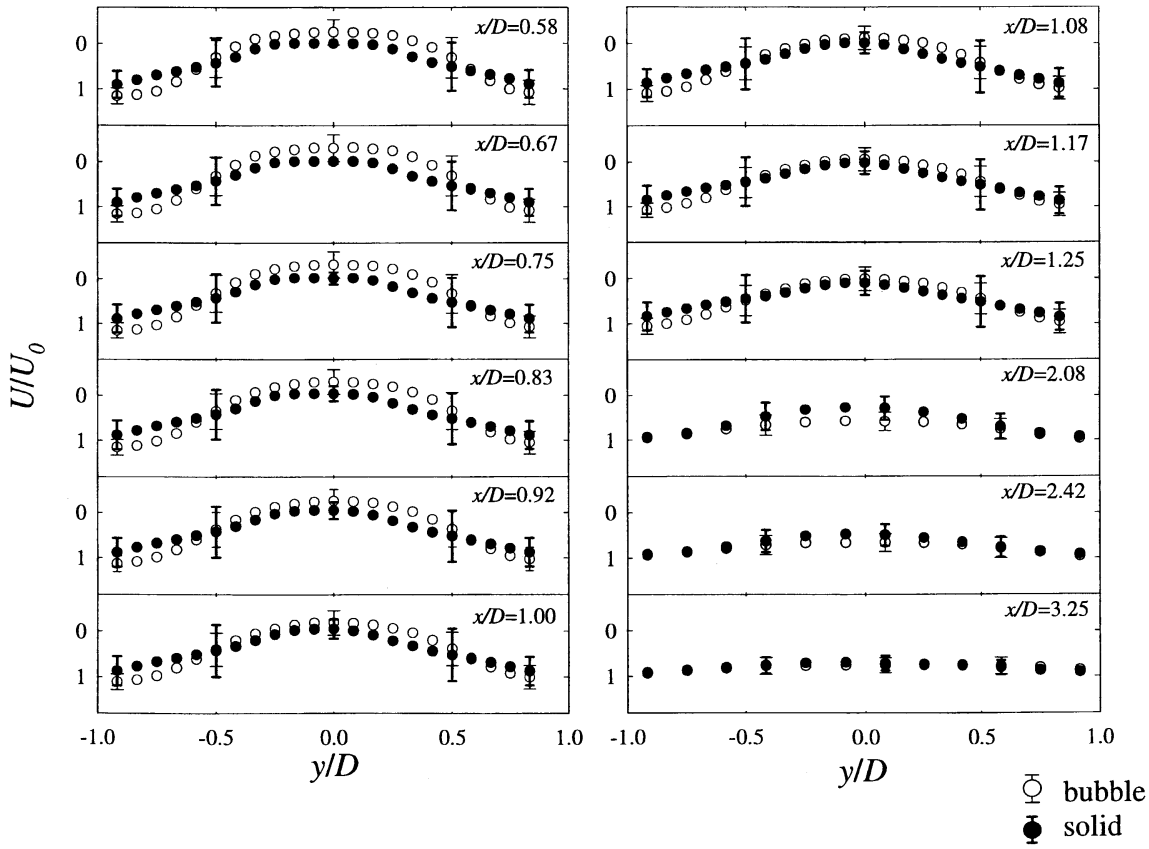

Fig. 7. The average velocity profiles, U/U_0, with downstream locations as parameter.

uncertainty is introduced, with respect to the calculated vectors, to the right of the solid or bubble. That is, due to total and partial shading, respectively, in the cases of the solid and bubble, the error in this right region is larger relative to the rest of the field. So, vectors in this region appear deflected with respect to the co-linear vectors representing the free stream flow. In fact in Figs. 14–16 any vector in this region to the right of the solid or bubble, whose components were larger and smaller than the corresponding component from the left region was eliminated. As for differences in their respective flow fields, upon close scrutiny we note that the flow pattern and the spatial extent of the wakes are different. In case of the solid, reversed flow within the recirculation region is relatively more well defined in contrast to the bubble. Additional details are however, better depicted by the following profiles.

Figures 7 and 8 thus shows the distribution of the average (U/U_0) and normalized root-mean-square (u_{rms}/U_0) velocities. Here (and hereafter) U_0 represents the average entrance velocity upstream of the bubble or solid ellipsoid as measured by LDV. The coordinates, (x,y), are respectively the downstream (axial) and cross-stream (transverse) directions. To facilitate our discussion, nine axial locations close to the solid and bubble and three locations further away (x/D = 2.08, 2.42, 3.25) have been selected. D is taken as the equivalent diameter of the bubble, D_e = 9.12 mm. In each of these figures the blank and filled circles represent respectively

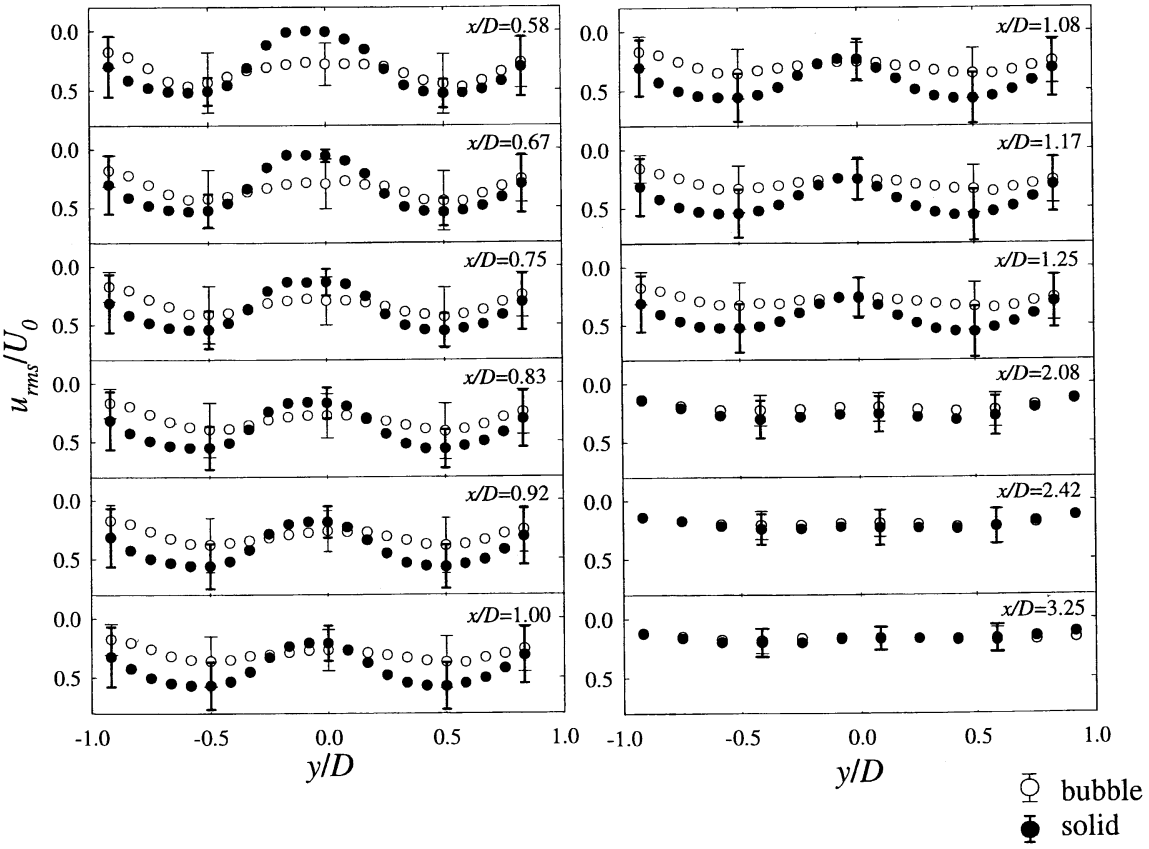

Fig. 8. The rms velocity profiles, u_{rms}/U_0, with downstream location as parameter.

the bubble and solid data. Also included in the figures are the typical error bars, at five y/D locations as follows: $y/D = 0.0, \pm 0.5$, and ± 1.0. The error bar represents one standard deviation calculated from a sample of 1000 velocity readings at each (x/D, y/D). The error bars are indicated in bold and un-bolded, respectively for the solid and bubble. We note that in Fig. 7 the velocity defects are very similar, symmetric and recover over a span of roughly $x/D \sim 3.25$, while in Fig. 8, the local maxima of u_{rms}/U_0 are located at $y/D \pm 0.5$. We know physically for both the solid and bubble that this is the location of the stagnation region to either side. Thus as expected the error bars are generally smaller at the center ($y/D \sim 0$) and at the ends of the region shown ($y/D \sim \pm 1.0$). As for contrasts between the solid and bubble, the fact that the error bars U/U_0 are of comparable magnitude may indirectly indicate similarity in the vorticity generation and conveyance mechanism. Naturally since the bubble oscillates inherently more than the solid, the error bars of (u_{rms}/U_0) are larger for the bubble in contrast to the solid.

In Figs. 9 and 10 we show the corresponding average (V/U_0) and normalized rms (v_{rms}/U_0) velocities. Also shown are the error bars as in the previous figure. Note here that in contrast to Fig. 7, in Fig. 9, the profiles is symmetric but of opposite sign (anti-symmetric) about the (vertical) centerline. This makes physical sense since on-average the flow to each side of the

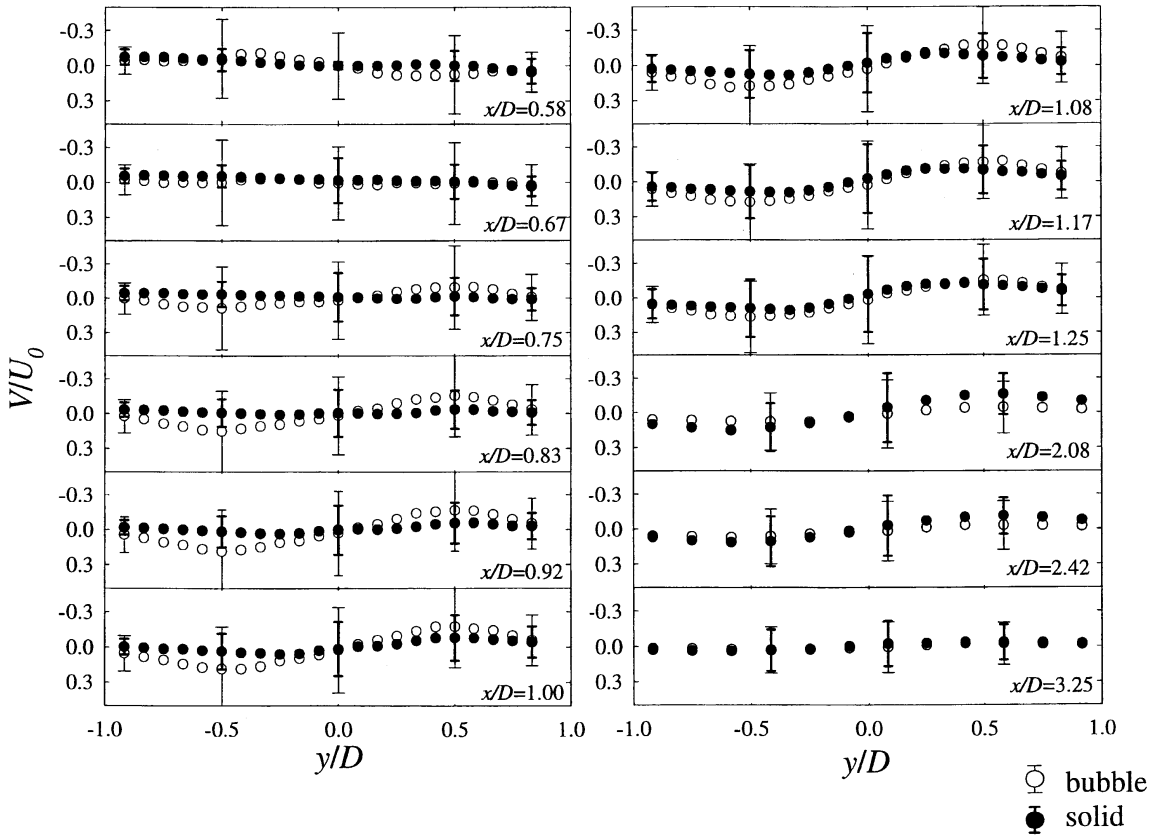

Fig. 9. The average velocity profiles, V/U_0, with downstream locations as parameter.

centerline is directed in opposite directions ($\pm y/D$). Note as well that due to the shedding mechanism common to both solid and bubble, a periodic transverse flow in the wake (see Figs. 14 and 15) and respectively, the wobbly motion of the bubble and constrained oscillation of the solid, the error bars here are larger than in Figs. 7 and 8.

While Figs. 8 and 10 show relative magnitudes of u_{rms} and v_{rms} with respect to U_0, Fig. 11 shows a direct comparison of the rms values along the streamwise direction with the cross-stream direction as parameter. Note that except at the centerline ($y/D = 0$) for $x/D < 0.75$ the bubble's oscillatory motion again contributes to a consistently larger v_{rms} than the solid. This makes physical sense. On the other hand, along the centerline region, $v_{\mathrm{rms}}/u_{\mathrm{rms}}$ shows as much as four times more fluctuation in the case of the solid. If one looks closely at v_{rms}, u_{rms} in Figs. 8 and 10, we see that both values are nearly zero for the solid. Thus we must be careful to interpret these results, as the uncertainly is as large as the v_{rms}, u_{rms} values themselves.

From the basic U, V, u_{rms} and v_{rms} data we subsequently derived the Reynolds stress and turbulent kinetic energy (tke) distributions. These are shown in Figs. 12 and 13 respectively. Note that the free parameter, x/D, are identical to those in the velocity plots while the convention of the Reynolds stress, $-\rho u'v'$, dictates our ordinate scale. The w'-component in the calculation of the turbulent kinetic energy has been assumed to be equivalent to the

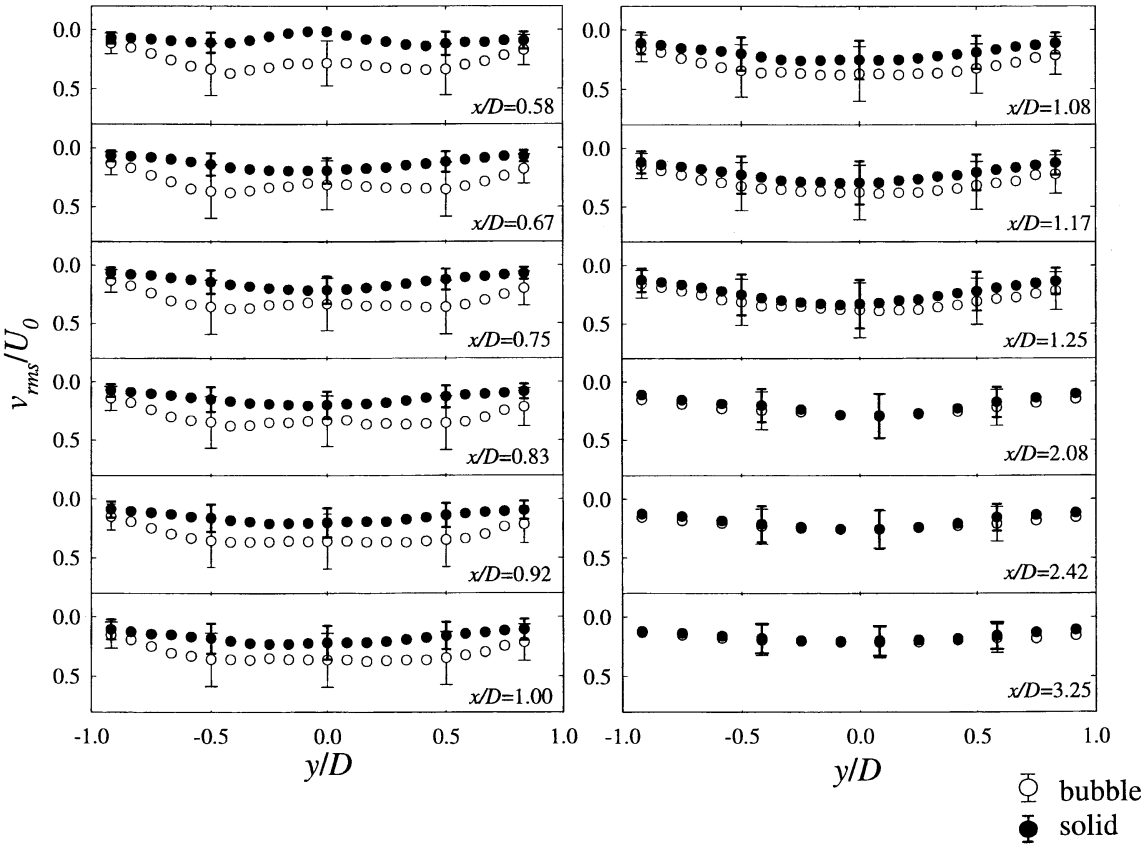

Fig. 10. The rms velocity profiles, v_{rms}/U_0, with downstream location as parameter.

v'-component since the oscillatory motion of the bubble should have no preferential (y or z) coordinate direction.

The data presented thus far show averaged quantities calculated from 1000 images. While these figures provide some insight, details of the flow field as dictated by the bubble's motion are overlooked. We thus present in Figs. 14 and 15 a sequence of vector field plots, at 50 ms intervals, respectively with the identified bubble's shadow image and that of the solid superimposed. The image sequence which was recorded with a normal speed (30 fps) VTR clearly depicts the change in shape and position of the bubble. However, in reality only captures snapshots of the bubble's continuous oscillatory motion which we judged to be approximately periodic every 200 ms. Note the change in the flow field with respect to the bubble's position at each 50 ms interval. In fact upon close scrutiny of the vector field in the figure, one can identify the vortices at each time frame and occasionally a shed vortex from one frame to another. Notice that shedding does not necessarily correspond to a spatially extreme (right or left) position of the bubble.

Fig. 15 shows a similar sequence for the solid. Notice that here the body is consistently identified in its constant shape but, also exhibits lateral (side-to-side) displacement which can be easily detected with respect to the square boundary. Although this flow-induced movement

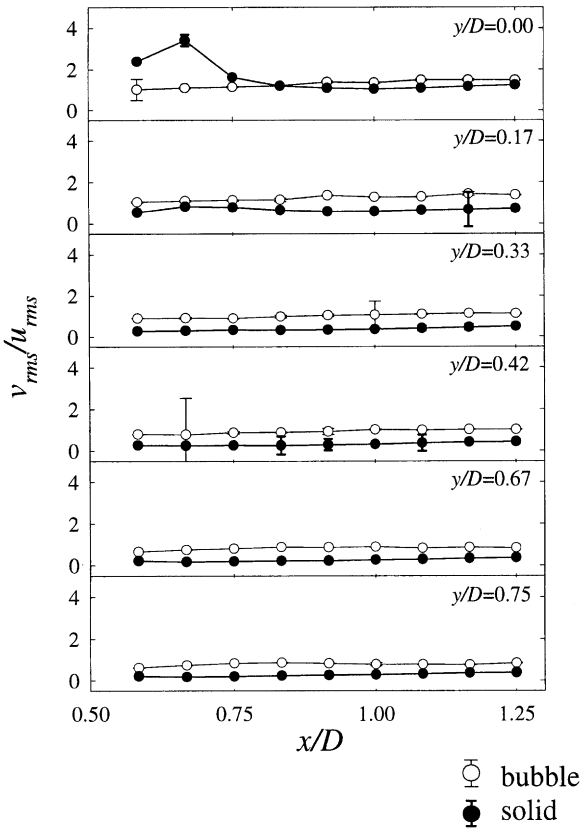

Fig. 11. Ratio of cross-streamwise to streamwise rms velocities.

may have influenced the solid's wake velocity field, we observed that in comparison to the bubble's oscillation frequency of 4.51 Hz, the solid's was approximately 1.67 Hz. We note that the in-plane (x–y plane) pendulum frequency, for the specified length of the needle, $f = (4\pi L/g)^{-1/2}$, was a comparable 1.78 Hz. We did not observe significant swinging in the y–z plane. Details on the oscillation frequency determination are given in the discussion. Notice in particular the differences in the spatial distribution and the typical size of vortices, as well as the significance of cross-stream flows in Figs. 14 and 15. Furthermore, because the bubble shape does change so drastically in time, we selected four representative types of bubble position from the sequence shown in order to selectively study its corresponding flow fields. We show these four types (type 0, 1, 2 and 3) in Fig. 16 and note that they typically represent the corresponding time events in Fig. 14 as follows: (1) type [flat] 300 ms, (2) type 1 [left-shifted] ~350 ms (or 0 ms), (3) type 2 [right-shifted] ~100 ms and (4) type 3 [full] ~50 ms (or 250 ms). The word in brackets gives their short descriptive names. In the figure, out of a total of 1000 images, each corresponding type of vector field plot is the average of the following number of images: type0-170, type1-350, type2-315, type3-155. The vector field of type 0 and 3 are symmetric and show a pair of vortices, while type 1 and 2 depict one dominant vortex situated near the elongated end of the bubble. Also shown with each type in bold solid line is

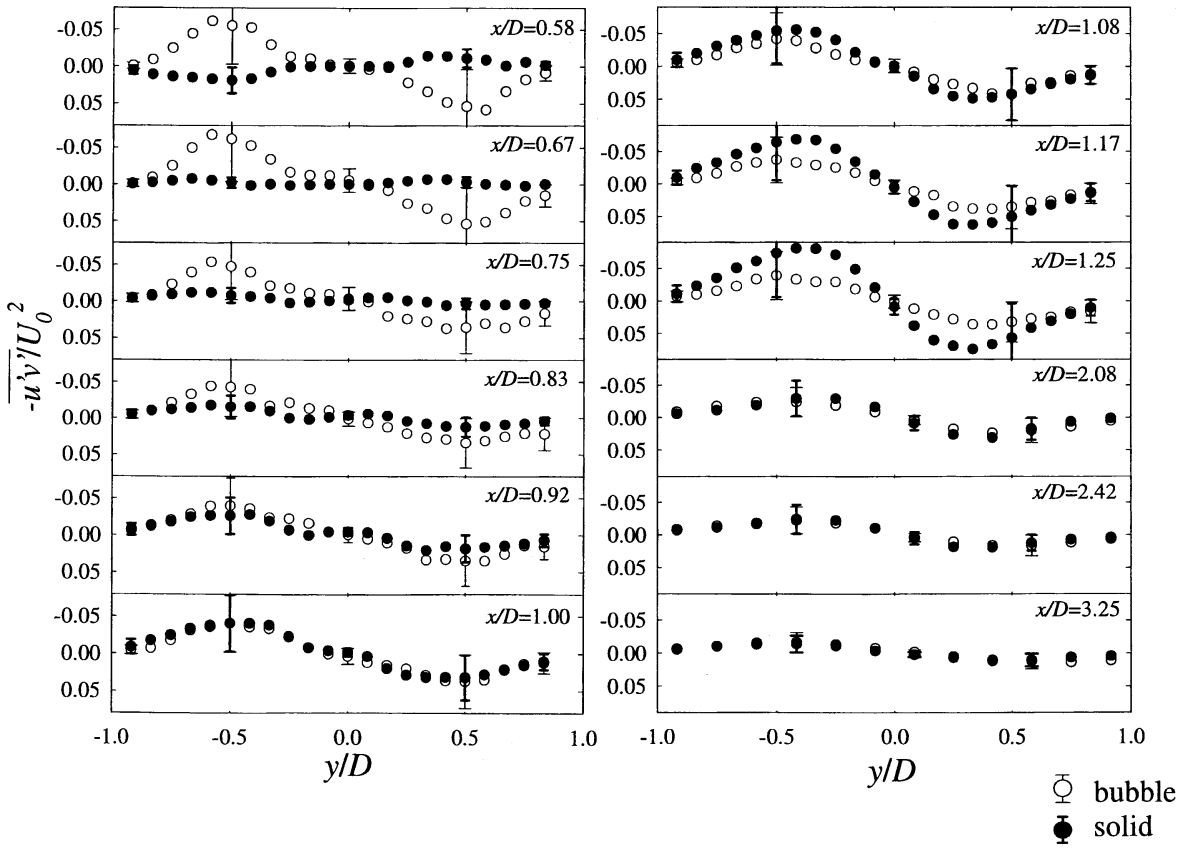

Fig. 12. Reynolds stress profiles with downstream locations as parameters.

the boundary of the vorticity flow region(s), a pair for types 0 and 3 and one each for types 1 and 2, and the location of its apparent center. This demarcation of the region will facilitate the discussions to follow.

We next show, in Fig. 17, the vorticity contours contrasting the bubble and solid. The sense of positive and negative vorticity are noted, respectively, by solid and dotted lines. Also shown in both figures are the previously identified vortical regions and their centers. One can see that besides the nearly symmetric distribution of vorticity about the central axis for both the bubble and solid, the contrasting feature is the denser set of isocontours and larger vorticity in the case of the bubble. Next in Fig. 18, we show the vorticity contours corresponding to the four bubble types shown in Fig. 16. Note here that the left-(type 1) and right-(type 2) shifted bubble orientations distort or respectively, 'pinch' the otherwise symmetric (type 0 and 3) vorticity distribution. There is also a relative lack of vorticity along the central axis of the wake as the flow coming from each side flow upward. If the density of isocontours and spatial distribution of vorticity is any indication of the turbulent kinetic energy in the wake, one may be inclined to say from the vorticity alone that the bubble's oscillatory motion influences the energy distribution. In fact, since both right and left-shifted orientations appear, one might predict that the oscillation contributes toward uniformity in the energy distribution.

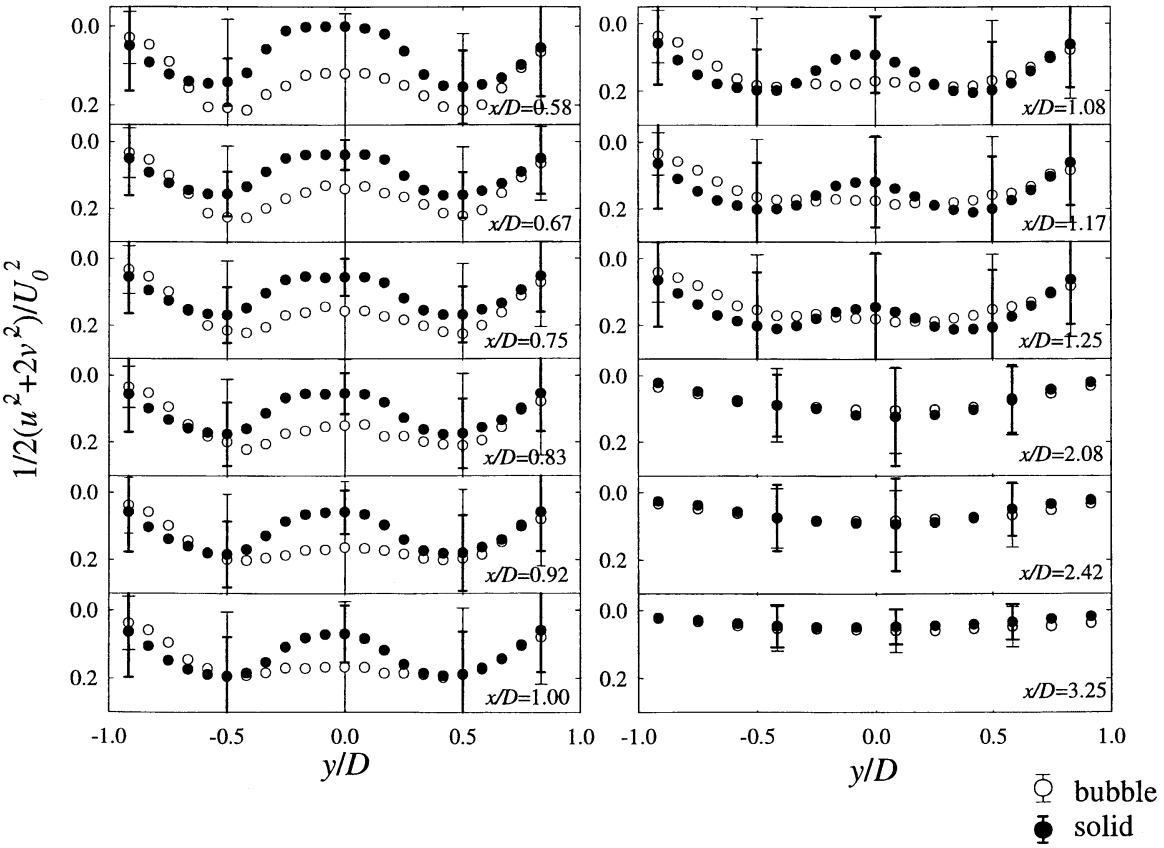

Fig. 13. Turbulent kinetic energy (tke) profiles with downstream locations as parameters.

In Figs. 19 and 20 we display the turbulent kinetic energy (tke) distribution contours corresponding to Figs. 17 and 18; that is, at first contrasting the bubble/solid and subsequently, for each of the four selected bubble types. The turbulent kinetic energy is here defined as $k = 1/2\ (u'^2 + 2\ v'^2)/U_0^2$ as v' and w' have been assumed to be equivalent. Note that although the contours are generally similar in shape, the tke isocontours are densely spaced and spatially more confined behind the solid than the bubble. We have also included in the figures the vortical regions and their centers as before. Finally, we have also shown in bold dotted lines the contour corresponding to the maximum and initial values of the vorticity taken from Fig. 17. The inclusions of these contours are intended to semi-quantitatively show the relationship between vortical flow regions, vorticity and tke.

4. Discussion

The results, as presented, appear to fulfil much of our first objective; that is, the combined use of DPIV, LIF and the above-described infrared shadow technique (IST) enables one to identify both the motion of a shadow of the body and the flow field around it simultaneously.

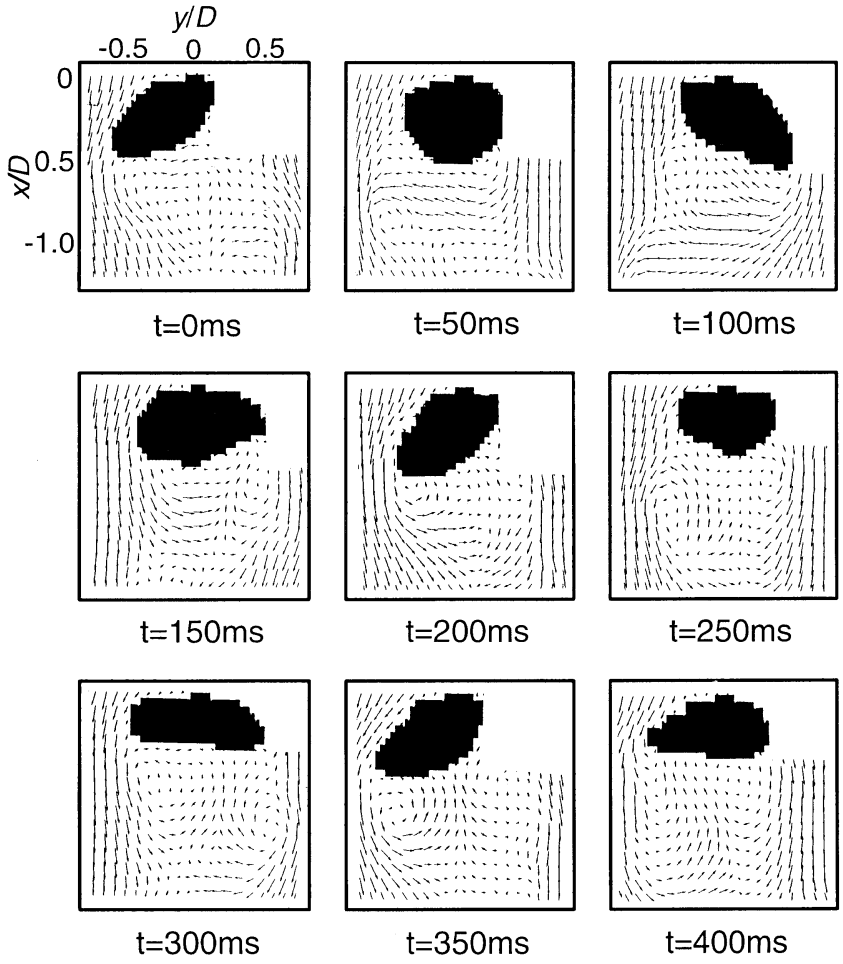

Fig. 14. Sequence of DPIV, LIF and IST produced velocity vector field and shadow-images detailing the bubble's oscillatory motion, taken at 50 ms intervals.

The measurement technique as implemented does have its limitations and associated errors. First, the gyrating bubble motion and the flow field are three-dimensional (3D). However, both the measured velocity field and the shadow of the body are essentially two-dimensional. These are limitations of our (2D) DPIV system and that in general of projected images, respectively. In fact, we cannot deny that due to the 3D nature of the flow field, the image of the bubble as taken from the front and subsequently superimposed upon the velocity field, taken from the rear, may individually correspond to different measurement planes. This is an unavoidable physical limitation which may be partially resolved by implementing the IST from another perspective so that at least the position of the laser sheet with respect to the bubble is captured. At the moment however, at least the flow field and boundary motion are measured simultaneously. The DPIV error in the obstructed region, that to the right of the bubble, is obviously a region of higher relative error as the light intensity is lacking (and different) compared to the rest of the field. The laser sheet enters from the left. As mentioned, we have

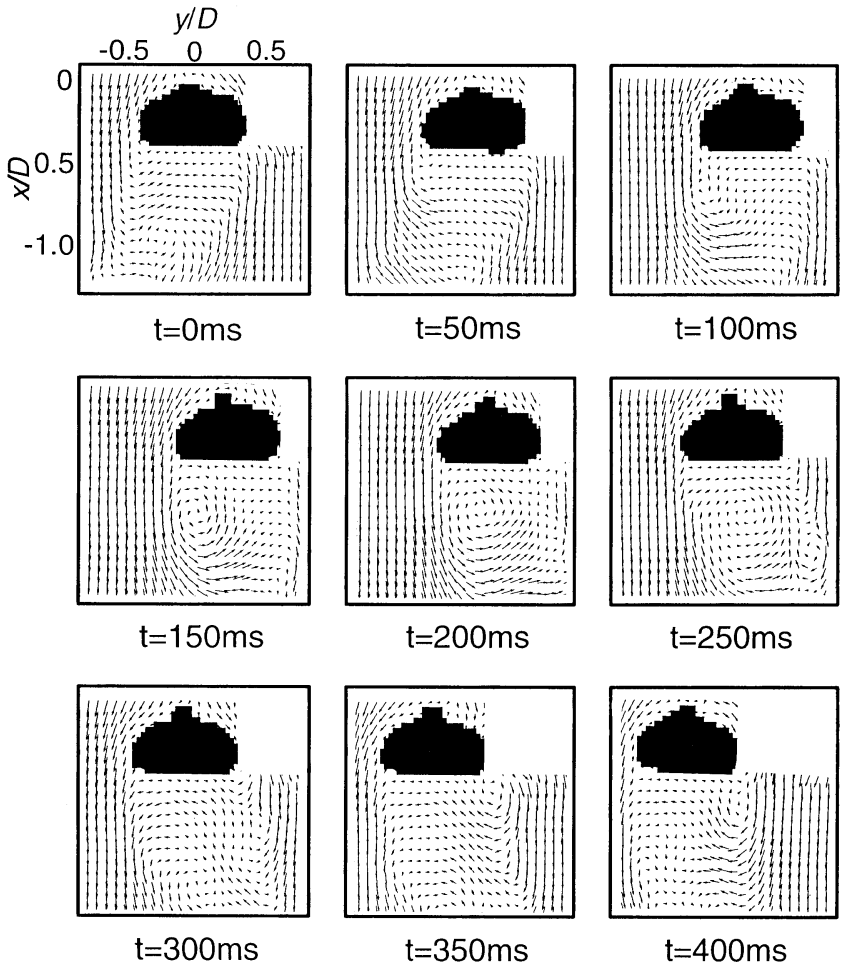

Fig. 15. The equivalent sequence using DPIV, LIF and IST for the solid.

omitted the data in this region. As for the shadow image, the estimated projection error is approximately 4% which we calculated based on the following method. We placed objects of known and measured cross-sectional area in the test section with the experimental loop operated as for the bubble and solid. We then compared the IST-produced image, under experimental conditions, with the actual dimensions.

Regarding the error of our DPIV system, we first show in Fig. 21 a simplified schematic of the PIV data analysis methodology. In this particular application of PIV we require two consecutive images containing the image of particles contained in and moving with the flow. We wish to 'track' the movement of each particle from one image frame to another. In order to apply the cross-correlation method one thus begins with a reference matrix (black dots represent particles) at time t and then scans a corresponding matrix taken a 'short' tome later $(t + \Delta t)$. The location of the corresponding matrix with respect to the reference is approximately known a priori since inherent in the assumption of the methodology is that the reference image only changes 'slightly'. In our application the images themselves are digitized

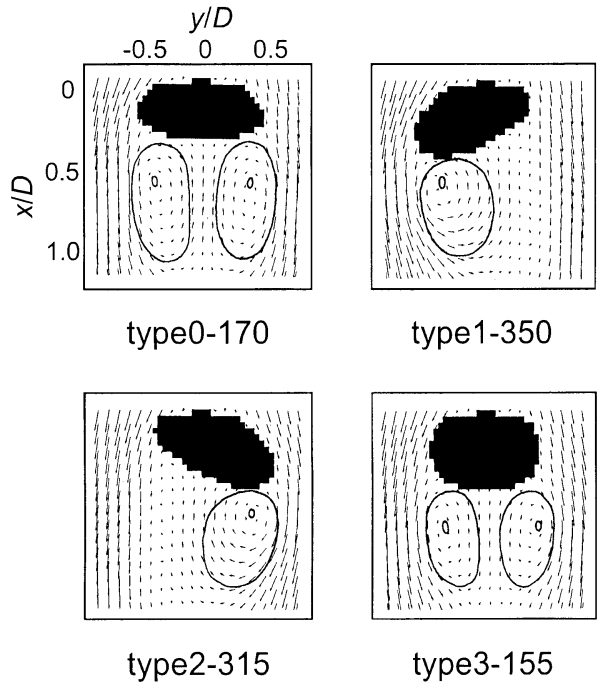

Fig. 16. The four bubble types along with its average velocity vector field.

and are thus encoded as gray-scale pixels; the matrix coefficient of cross-correlation between say a 'particle pixel' in the reference (time t; black dot) to that in the corresponding matrix identifies its most likely location ($t + \Delta t$). The velocity vector is then evaluated from the displacement and time interval between the two frames. The size of the correlated area is left as a variable since the optimum size is directed by the density of tracer particles and local strain rate of the flow field. In general the poorest cross-correlation results if the density of particles is low and the flow contains large vorticity and shear; that is, erroneous vectors can be produced due to difficulty in identifying a distinct maximum correlation coefficient. In this case a verification procedure consisting of calculating the vectors over the entire plane (of the

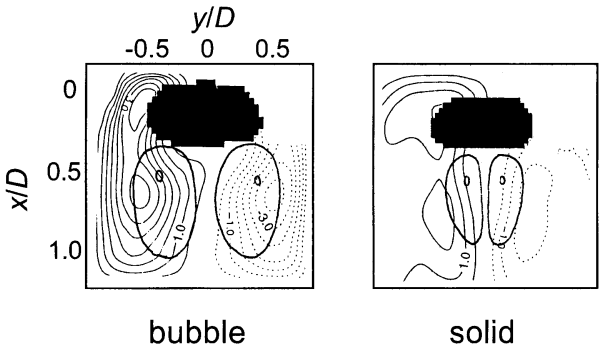

Fig. 17. Vorticity contour contrasting the bubble and the solid.

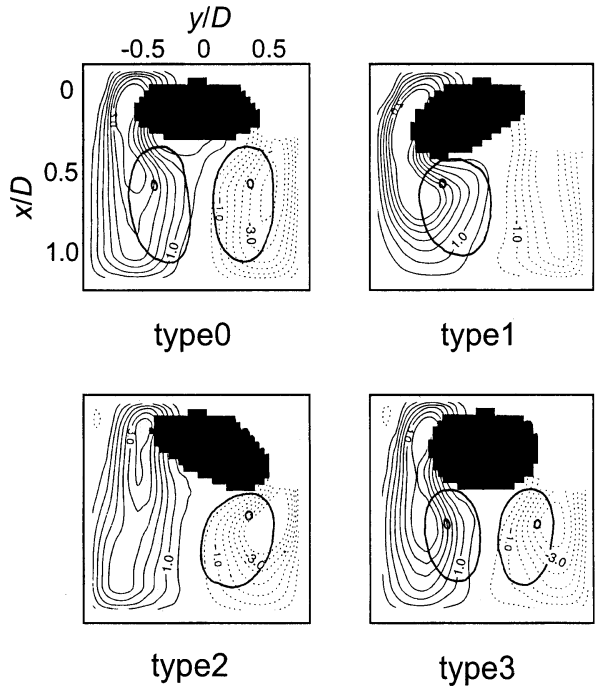

Fig. 18. Vorticity contour corresponding to the four selected bubble types.

image) while storing in memory the second and third highest correlation values and displacements was implemented. If a given vector is considerably different from an 'average' vector calculated from its surrounding vectors, the most similar vector with the second or third highest correlation is then selected. This procedure is repeated a number of times over the entire vector field. If there are still a number of 'inconsistent' vectors, then these vectors are recalculated with an enlarged reference matrix. If an alternate or 'preferable' vector results from this re-calculation, then it replaces the previous vector. The re-calculation is repeated to correct all the remaining erroneous vectors. With the so-described PIV data analysis technique the calculated error in magnitude (of velocity) with respect to $U_0 = 24.5$ cm/s as reference was

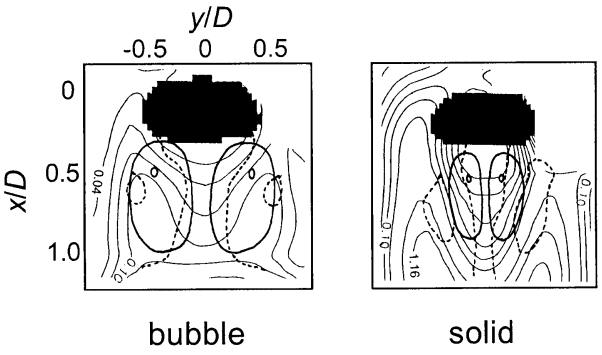

Fig. 19. Turbulent kinetic energy contour contrasting the bubble and the solid.

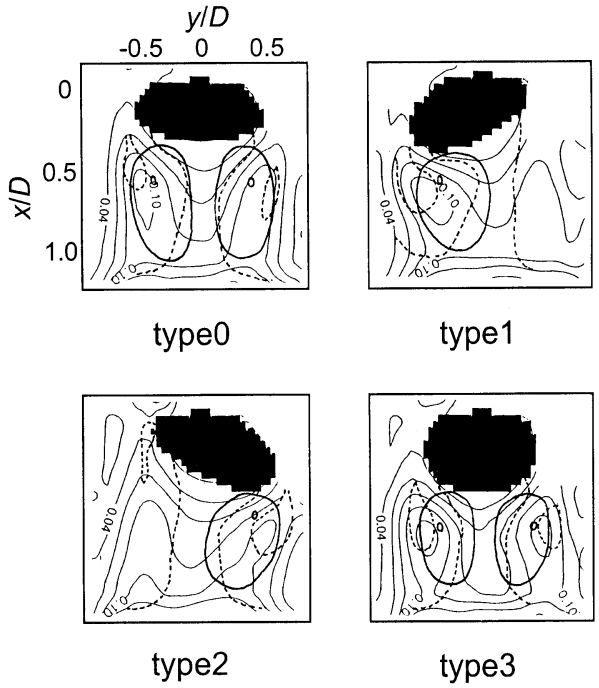

Fig. 20. Turbulent kinetic energy contour corresponding to the four selected bubble types.

$\pm$3.4%. In other words the error in magnitude corresponds to $\pm$8.3 mm/s. In terms of the total number of vectors, typically 245 in Fig. 14, there were 27 'inconsistent' vectors (directional inconsistency) which upon re-evaluation were reduced to 15 possible error vectors (6.1%).

Before discussing the solid/bubble shadow projections and their respective flow fields we address the influence of the disk onto which the bubble attaches itself. For a disk and bubble equivalent diameter range, $1 \leqq D_{\text{disk}} \leqq 2$ mm and $9 \leqq D_{\text{disk}} \leqq 12$ mm, the cross-sectional area ratio can be as little as 2.8% or as much as 19.8% of the area of the bubble. In the former

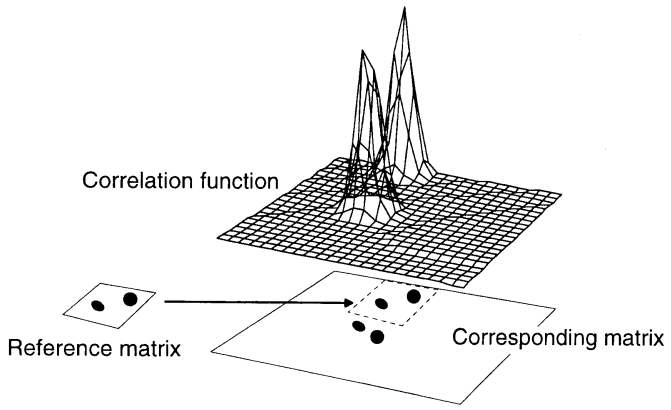

Fig. 21. Schematic diagram of PIV cross-correlation methodology.

case the potential influence is within the measurement error. In the latter case it is plausible that the influence is within the measurement error. In the latter case however, it is plausible that the flow along the disk may influence the flow around the rest of the bubble's surface. Nevertheless, the flow field resulting from the shedding at the stagnation point and separately, interaction with the oscillating tail are still defined by the gas–liquid interface. The surface tension at the disk–bubble–water interface constrains the interfacial movement along its periphery and any surface deformations (waves and instabilities) that may cross the central regions. It has been assumed that the influence of the disk on the shedding and oscillating tail mechanisms are minor and the differences (with and without disk), if they can even be detected (measured), are small.

We next turn to a discussion of the bubble motion and the flow field with which it interacts. It can be said that the bubble under the current configuration and flow conditions oscillate or gyrate; that is, the base of the bubble rocks back-and-forth in a manner characteristic and consistent with the estimated Reynolds and Eotvos numbers. The Reynolds number is based on the equivalent diameter of the bubble and its rise velocity or in our case the average downward liquid velocity ($U_0 = 24.5$ cm/s). The Eotvos number is based on the equivalent diameter and thermophysical properties of water at 15°C and 20°C. We estimate the *Re*-number range to be, $1950 < Re_{De} < 2250$, and thus according to Fan and Tsuchiya (1990) the flow in the wale is turbulent. The *Eo*-number is approximately, $11 < Eo < 11.5$; thus the bubble is in the 'wobbling' region according to Clift et al. (1978). We have referred to this as 'oscillating' or 'gyrating'. For this Reynolds range (and others), Fan and Tsuchiya (1990) have described in detail, having reviewed many past investigations, the vortex shedding mechanism and the wake flow associated with bubbles and solids. Although the detailed mechanism of vortex shedding is of great interest, DPIV data collected at a normal framing rate of 30 fps cannot provide the necessary sequence of vector field plots needed to study the shedding phenomena in detail. In other words, although the phenomena occurs periodically but during a short time span, at 30 fps we can only capture glimpses of the shedding process. For this reason we have mainly presented data averaged over 1000 images in Figs. 7–13 and draw semi-quantitative conclusions from Figs. 14–20.

Given a Reynolds number range we can confirm the validity of our observation regarding the bubble's oscillation shedding frequencies by estimating the Strouhals (*Sr*) number. We see from past experimental data of *Sr* vs *Re*-number that our corresponding Strouhal number for vortex shedding is approximately $0.15 < Sr < 0.20$ [Cf: Tsuchiya and Fan, 1988]. An equally separate calculation of the *Sr*-number based on an estimate of the bubble's oscillation frequency from high-speed video images yields $0.16 < Sr < 0.245$. Here we assume that the bubble oscillation and vortex shedding frequencies are equal (locked-in) and acknowledge that usually the *Sr*-number is based on the vortex shedding frequency. We thus see that the magnitudes roughly agree. Regarding the oscillation frequency of the bubble (surface), it was estimated visually as follows. An image sequence of bubble projections was first scanned with respect to a starting image for similar projections at some later time. The shortest interval between images was in this case, 8.33 ms (120 fps). Once several likely candidate images were selected, a square grid made up of 5×5 (mm^2) square segments was superimposed on the starting and candidate images. The boundary of the bubble was then identified with coordinates, (x,y), assigned to each square as on a geographical map, for each of the images. A

determination of the frequency was then simply based on the candidate image with the highest fraction of boundary elements in comparison to the starting image. Then to counter possible bias from a given starting image, different starting images were selected. From this simple and semi-quantitative boundary identification scheme we arrived at an average oscillation frequency of 4.51 Hz with one standard deviation of 0.36 Hz.

Having confirmed the characteristic motion of our bubble, we turn to the flow field in the wake. In order to facilitate our discussion, we take as given the vortex shedding mechanism for both the bubble and solid. Thus the generation of vorticity near the flow separation point along the edge of their respective boundaries, the conveyance of vorticity along the nearby free shear layer, the formation of a circular vortex (two-dimensional) or vortex ring (three-dimensional) in the wake and eventual shedding of vortices by an entrained cross-flow are taken to be common to both the solid and bubble. The source of any contrast in their respective wake flows are, therefore, due to a difference in shape deformation, slip versus non-slip, and the effective mass. In the case of the solid, the investigation by Cantwell and Coles (1983) on entrainment and turbulent flow in the wake of a cylinder provides substantial reference data, though different geometrically, at least in terms of data presentation. That is, plots of the velocity vector field, along with Reynolds stress and tke contours are presented. In their work, velocity measurements were taken with a rotating X-array hot-wire probe placed on a traversing mechanism that moved in the downstream direction. One of the main conclusions of their work was that turbulence is produced by vortex stretching near the saddle points in the flow field; that is, by stretching of small-scale vorticity oriented along the diverging separatices. In Fig. 22 we have taken the liberty to sketch some of these flow features. Fortunately in their work, the saddle points of the vector field are relatively easily identified as there are only four saddle points located over eight diameters of the wake. One can, subsequently, see that the tke production has a maximum near these saddle points. In the present case, however, the continuous motion of the saddle point made the task of identifying it, though possible in some instances, impossible in others. We were thus unable to construct a time-sequence of vector plots with identifiable saddle points as we wished. We nevertheless know that the region of interest in comparing the wake flow behind a bubble and solid ellipsoid is approximately within 1.25 diameters of the coordinate axes as Figs. 7–13 show. That is, beyond $x/D > 1.25$ the profiles are very similar. Moreover, we can semi-quantitatively correlate tke production to our velocity data by identifying regions inherent in both wakes, such as the vortical flow region and then transposing these regions in similarly-scaled vorticity and tke contour plots. This is fact the reason for identifying the vortical flow regions in Fig. 16 and subsequently noting them in Figs. 17–20.

Looking first at the Reynolds stress development with downstream distance however, some differences are already additional differences become apparent. In contrast to the solid, which has a quasi-steady Re-stress distribution up to $x/D \sim 0.75$, the bubble clearly has a 'near-wake' defined by an anti-symmetric Re-stress profile (Fig. 12) over the same x/D distance. Then up to approximately $x/D \sim 0.92$, the bubble's anti-symmetric profile decays whereas for the solid, an equally anti-symmetric profile develops between $0.92 < x/D < 1.25$. Interestingly enough, the bubble's Re-stress profile recovers beyond $x/D > 0.92$ so that a second anti-symmetric profile appears analogously to the solid's. Although the solid and the bubble oscillate at different amplitudes (direction) and frequencies, it is plausible that the physical mechanism responsible

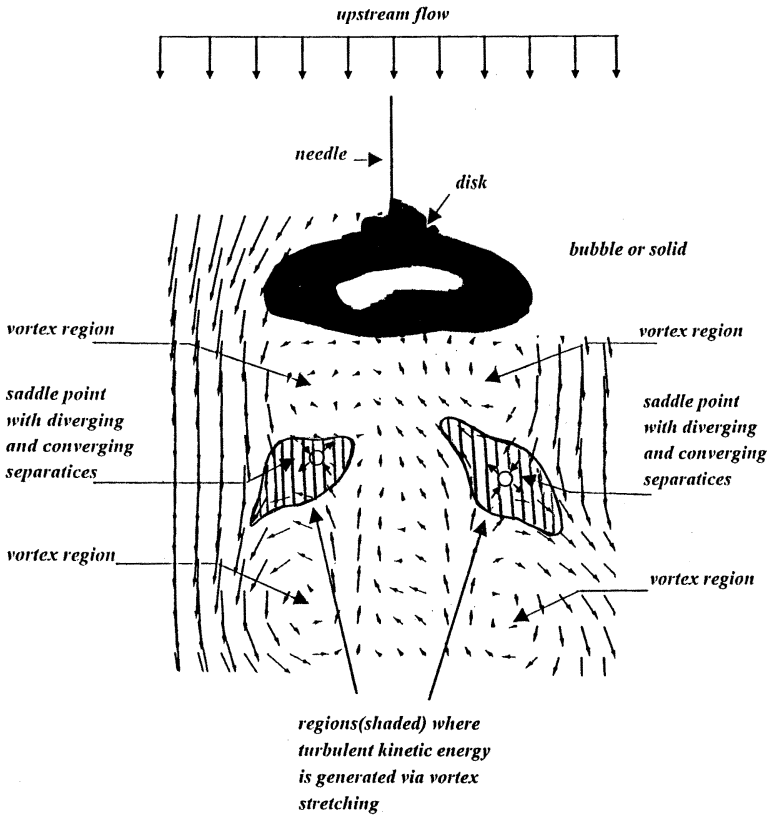

Fig. 22. Schematic of saddle points and separatices in the wake of a bluff body.

for the *Re*-stress profile development between $0.92 < x/D < 1.25$ for both the bubble and solid, have common physical origins. On the other hand, the near-wake *Re*-stress profile in case of the bubble is likely due to its oscillatory motion of the tail. When we thus look for a correlation between *Re*-stress (Fig. 12) and tke (Fig. 13), we find evidence that a finite and established *Re*-stress gradient in the wake, such as at $0.58 < x/D < 0.83$, contribute toward an uniformity of the tke distribution as shown by the trend in Fig. 13 for $0.58 < x/D < 1.25$. This is clearly not the case of the solid.

The contour plots support the same conclusions. In Fig. 16, the bounds of the two vortices, in other wards the vortical flow regions and the location of the apparent center or minimum value for each bubble type are as drawn. In Figs. 17–20 we then show the vorticity and tke contours respectively with these identified vortical flow regions in bold. As expected for the solid and bubble vorticity is generated along the stagnation region at each side of the bubble/solid. An isocontour representing a relative maxima is clearly indicated. A second maxima is also depicted downstream, though different in location and extent (area) for the bubble and solid. In particular the concentrated set of isocontours in the bubble's near wake ($x/D \sim 0.5$, $y/D < 0.5$), may partially be attributed to the deformation (elongation and axial movement) of the bubble's shape itself since as noted, both the bubble and solid oscillate in the transverse direction in shape generates vorticity in the near wake of the bubble. It is therefore not surprising that the vortical flow regions are located within the near-wake isocontours and

though slightly offset, the 'center' of the vortex corresponds in position to the second local maximal isocontour. This also holds true for bubble position type 1 and 2 in Fig. 18. In fact it appears that the extreme positions (type 1 and type 2) generate vorticity across the near wake. On the other hand there is no such mechanism in the case of the ellipsoid. Thus for the solid vorticity is generated along the outer edge of the vortical regions where the flow is accelerated and the vortex is stretches downstream.

Consequently in Figs. 19 and 20 the tke isocontours of the bubble are more uniformly distributed than the solid. If vortex stretching does indeed extract energy from the mean flow most efficiently, the influence of bubble position type 1 and 2 is to distribute this energy toward the center of the near wake. Furthermore as a result of the elongation of the bubble the isocontours representing relatively large tke values extend transversely in the near wake. The composite effect of the bubble's oscillatory motion and shape distortion is thus a more widely spaced set of isocontours behind the bubble and an approximate concurrence of the maximum vorticity, vortex center and the maximum tke isocontour. In the case of solid however, lacking shape distortion and substantial oscillation, vorticity stretching and thus tke generation only appears along the outer edge of the vortices since this is the region where the flow is accelerated. So, contrary to its appearance the densely spaced isocontours in the near wake of the solid, as Fig. 13 confirms represents a stepwise decrease in the tke magnitude. In a three-dimensional sense, the concentration of isocontours in the near-wake of the solid ($0.5 < x/D < 1.0,\ y/D \pm 0.5$) thus represent a 'valley' while the two peaks are located at $x/D \sim 1.0,\ y/D > \pm 0.5$.

This then brings us to the present limitations of our measurement method and the results as presented. In that one of our ambitions was the elucidation of the difference in turbulent wake structure behind a bubble versus its solid ellipsoid, we realized that some further quantification of the field-type plots, mainly vector, vorticity and tke, are needed in order to establish a definite correlation. In this respect, efforts are underway on DPIV at 120 fps or greater so that saddle points and vortex shedding can be more precisely identified. We also note that because our solid ellipsoid has a specific gravity grater than unity, the ellipsoid does not assume conditions approaching a free fall. Thus in order to truly simulate the bubble, but with a solid boundary condition, we are conducting measurements with a hollow solid. Finally we recognize that quantifying the bubble's motion by an IST from a second perspective would contribute toward the proper identification of the motion and facilitate the task of correlating the flow field to the projected shadow positions.

5. Conclusions

Using DPIV supplemented by LIF and an infrared shadow-image technique (IST) produced by an array of LEDs shining through a translucent window, two CCD cameras were use to simultaneously identify the boundary (shape) and flow field around a bubble and separately an ellipsoid with a flat bottom. The bubble assumed a wobbly, ellipsoidal shape consistent with estimates of the equivalent diameter (D_e) based Reynolds and Eotvos numbers. The solid ellipsoid was geometrically similar to the time-averaged shape of the oscillating bubble. The bubble or solid was suspended in the middle of a square channel in which water flowed

downward through a grid at an average velocity nearly identical to the terminal velocity of a freely rising bubble of the same D_e. From a collection of 1000 images, boundary and velocity information were extracted. A comparison of first the vector flow field around the solid and bubble revealed differences in the wake flow structure as expected; that is, the implemented measurement system could detect differences in the wake flow field resulting from, respectively, an oscillating bubble with slip at the interface and a solid with no slip at the surface boundary. Upon scrutinizing the average velocity, rms-velocity, u_{rms} and v_{rms} ratio, vorticity and turbulent kinetic energy contours and finally the Reynolds stress distributions, we noted that indeed the bubble's oscillatory motion is responsible for two phenomena, these begin: (1) the generation of vorticity in the near-wake, meaning less than one equivalent diameter; and (2) as a result of its motion, the likely stretching of vorticity such that turbulent kinetic energy is more uniformly distributed in the near wake in comparison to the solid ellipsoid of nearly the same equivalent diameter.

Acknowledgements

The first author expresses his sincere appreciation to Professors M. Maeda and K. Hishida for providing the opportunity to conduct this experiment and thanks to Mr K. Iizuka, M. Maekawa, and Ms A. Fujiwara for conducting the experiments and processing the data. The first author is also grateful to Professor P. S. Lykoudis at Purdue University for his ideas regarding a similar experiment, some elements of which was used in the present work. This work was subsidized by the Grand-in-Aid of Japanese Ministry of Education, Science and Culture (grant no. 08405019).

References

Cantwell, B., Coles, D., 1983. An experimental study of entrainment and transport in the turbulent near wake of a circular cylinder. Journal of Fluid Mechanics 136, 321–374.

Clift, R., Grace, J.R., Weber, M.E., 1978. Bubbles, Drops and Particles. Academic Press, New York.

Davidson, J.F., Kirk, F.A., 1969. Holding a bubble fixed by downward flow. Chemical Engineering Science 24, 1529–1530.

Fan, L-S., Tsuchiya, K., 1990. Bubble wake dynamics in liquids and liquid-solid suspensions. Butterworth-Heinemann Series in Chemical Engineering, Boston (USA) isbn 0-409-90286-1.

Kojima, E., Akehata, T., Shirai, T., 1975. Behavior of single air bubbles held stationary in downward flow. Journal of Chemical Engineering of Japan 8 (2), 108–113.

Levich, V.G., 1962. Physicochemical Hydrodynamics. Prentice-Hall, Englewood Cliffs, New Jersey.

Moo-Young, M., Fulford, G., Cheyne, I., 1971. Bubble motion studies in a countercurrent flow apparatus. Industrial Engineering Chemical Fundam. 10 (1), 157–160.

Sakakibara, J., Hishida, K., Maeda, M., 1993. Quantitative visualization of convective heat transfer near the stagnation region of an impinging jet. Experimental Numerical Flow Visualization FED-Vol. 172 (ASME), 93–99.

Sakakibara, J., Hishida, K., Maeda, M., 1993. Measurement of thermally stratified pipe flow using image-processing techniques. Experiments in Fluids 16, 82–96.

Tadaki, T., Maeda, S., 1961. On the shape and velocity of single air bubbles rising in various liquids. Chemical Engineering 25-4, 254–264 (in Japanese).

Tsuchiya, K., Fan, L-S., 1988. Near-wake structure of a single gas bubble in a two-dimensional liquid–solid fluidized bed: vortex shedding and wake size variation. Chemical Engineering Science 43 (5), 1167–1181.